International Journal of Nanomedicine

Dovepress
open access to scientific and medical research

Open Access Full Text Article

ORIGINAL RESEARCH

Combined UTMD-Nanoplatform for the Effective Delivery of Drugs to Treat Renal Cell Carcinoma

Ting Dai*, Qimeihui Wang*, Lingyu Zhu, Qiang Luo, Jiayu Yang, Xia Meng, Hui Wang, Zhixia Sun

Department of Ultrasound, China-Japan Union Hospital of Jilin University, Changchun, Jilin Province, People's Republic of China

*These authors contributed equally to this work

Correspondence: Hui Wang; Zhixia Sun, Department of Ultrasound, China-Japan Union Hospital of Jilin University, Changchun, Jilin Province, 130033, People's Republic of China, Email whui66@jlu.edu.cn; sunzx@jlu.edu.cn

Introduction: The effective accumulation of nanoparticles (NPs) in the tumour area is an important goals of current nanotechnology research, and a targeted nanoplatform is an effective solution. So we designed a multifunctional sound-sensitive targeted NP that combines a sonosensitizer to enable precisely targeted, deep-penetration sonodynamic therapy (SDT) in combination with multimodal imaging for the diagnosis and monitoring of renal cell carcinoma (RCC).

Methods: ZnPP@PP NPs (ZnPP@PLGA- PFP NPs) were prepared via a double emulsion method, and G250 was covalently attached to the NPs shell via the carbon diimide method. Physicochemical property tests were conducted on the ZnPP@G-PP NPs, including tests of particle size, potential distribution, encapsulation efficiency and drug loading capability. We assessed the targeting ability, the production of reactive oxygen species (ROS) and permeability of the NPs in vitro. Moreover, we evaluated the nanoparticle's multimodal imaging capabilities and therapeutic ability against RCC, both in vitro and in vivo.

Results: The Znpp@G-PP NPs were successfully constructed, and their general properties showed uniform particle size, negative potential and good stability. The nanoparticles were successfully loaded with ZnPP and connected with G250, showing tumor-specific targeting ability. Under LIFU irradiation, the nanoparticles produced $^1O_2$ by SDT. For RCC, PA/US multi-modal imaging of Znpp@G-PP NPs provide diagnostic information and monitor therapies in real time in 786-O RCC xenografts, with good biocompatibility. With the UTMD, nanoparticles can be effectively targeted into the tumor cells and penetrate into the tumor interior, significantly improving the SDT effect. Experiments in vitro and in vivo showed that the combination of the nanoparticles and LIFU could suppress the tumor, and the therapeutic effect was confirmed by immunohistochemistry.

Conclusion: ZnPP@G-PP NPs provide a promising theranostic strategy for RCC and a platform for further research on improving the efficacy of diagnosis and treatment.

Keywords: targeted therapy, deep-penetration, sonodynamic therapy, multimodal imaging

Introduction

Renal cell carcinoma (RCC) is one of the most common malignant tumors of the kidney, with the clear cell renal cell carcinoma (ccRCC) subtype accounting for the majority of cases.[1,2] ccRCC possesses a certain degree of malignancy and may, under certain circumstances, exhibit early metastasis.For patients with advanced or metastatic disease, the efficacy of surgical treatment may be limited, and traditional radiotherapy and chemotherapy have not shown significant effectiveness against ccRCC, which can affect patient survival.[3–5] Currently, existing imaging technologies have clear limitations in the early diagnosis of ccRCC. Therefore, researching and developing new diagnostic and therapeutic strategies are crucial for improving the early diagnostic accuracy and treatment outcomes of ccRCC.

Nanotherapy has provided innovative opportunities in the medical field; however, precisely delivering NPs to target lesions remains challenging.[6,7] Passive targeting primarily relies on the enhanced permeability and retention (EPR) effect, exhibiting an extended residence time in tumor tissues. However, due to potentially low accumulation levels, this

Received: 17 January 2024
Accepted: 1 August 2024
Published: 21 August 2024

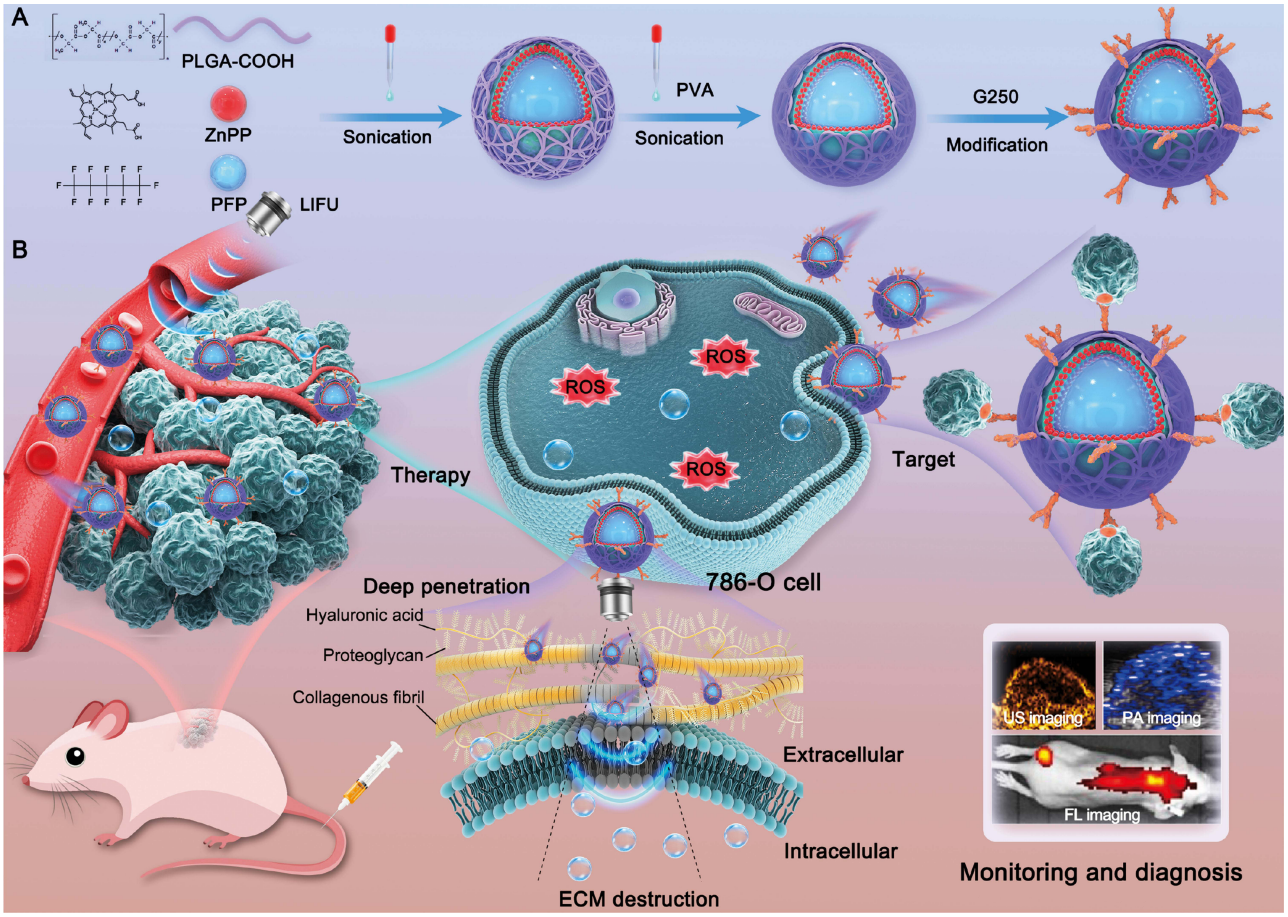

Scheme 1 Schematic illustration of ZnPP@G-PP NP synthesis (**A**) and the efficient accumulation of ZnPP@G-PP NPs in 786-O tumour cells, achieving targeted penetration and multimodal imaging-guided diagnosis and monitoring under sonodynamic action (**B**).

approach can sometimes reduce therapeutic efficacy and potentially increase the toxic side effects of the drug. In contrast, active targeting technology significantly enhances the accumulation efficiency and concentration of NPs in tumor tissues by utilizing specific targeting molecules that bind to receptors on the surface of tumor cells. This not only improves therapeutic outcomes but also achieves more precise tumor treatment and reduces adverse effects on normal tissues.[8] G250 is a protein that is overexpressed on the surface of ccRCC tumour cells and serves as a tumour-associated antigen.[9–14] By using antibodies specific for G250, NPs can be specifically targeted to tumour tissues and can efficiently deliver their cargo, thereby increasing the precision and efficacy of treatment.

Owing to their unique microenvironment, solid tumours, especially those with surfaces that are rich in extracellular matrix (ECM) structures such as collagen fibres, hyaluronic acid matrices, and proteoglycans, have a physical barrier that greatly limits the effective delivery of NPs. To overcome this challenge,[15–19] SDT offers an innovative solution. LIFU can generate thermal and mechanical effects,[20,21] effectively disrupting the ECM structures in the tumour microenvironment[22–24] and increasing the effective accumulation of NPs. LIFU has precise focusing capability, allowing the quantitatively controlled release of drug delivery systems without damaging surrounding normal tissues.[25,26] Compared with traditional diagnostic US, LIFU exhibits excellent penetration and attenuation resistance, and it does not result in toxicity in normal tissues.[27,28] Additionally, UTMD is an active targeting strategy that utilizes the interaction between US waves and microbubbles(MBs) for precision treatment of diseased tissues through cavitation phenomena. This technology is widely used to promote gene transfection, facilitate drug delivery, and increase capillary permeability.[29–31] In UTMD, the use of US energy to destroy MBs that are formed by liquid perfluorocarbon compounds (PFCs) encapsulated in NPs increases tissue permeability and cell membrane permeability, thereby increasing the

delivery efficiency of NPs. Zinc protoporphyrin (ZnPP) is a sonosensitizer that produces ROS after activation by LIFU, resulting in strong cytotoxicity. ROS damage molecular structures such as DNA, proteins, and lipids in tumour cells, thereby achieving precise tumour cell death. ZnPP is used as a sonosensitizer not only because of its excellent sonodynamic therapeutic effect but also because of its PA characteristics, which allow the real-time monitoring and evaluation of treatment effects during therapy.

Multimodal imaging plays a crucial role in medical diagnosis and real-time assessment of treatment efficacy, ensuring the safety and effectiveness of treatments and helping to optimize the treatment duration.[32–35] Among multimodal imaging techniques, PA, US, and FL imaging play key diagnostic roles.[20] Among these approaches, PA imaging has high resolution, FL imaging can reveal the details of NPs distributions in real time with high sensitivity, and US waves can penetrate deep tissues, revealing dynamic tissue structures and blood flow states. Integrating these imaging technologies (PA, FL, and US) into a multifunctional nanoplatform not only overcomes the limitations of single imaging techniques but also has considerable application potential in treatment monitoring and precision diagnosis of ccRCC.[36]

In this study, we developed a nanoparticle based on poly(lactic-co-glycolic acid) (PLGA) as the carrier. The NPs were loaded with the sonosensitizer ZnPP and encapsulated with perfluoropentane (PFP). To increase the targeting ability, we modified the surface of the NPs with G250. By combining these NPs with multimodal imaging techniques, we successfully developed a strategy for precision targeted therapy of ccRCC and evaluated its effects. The accumulation of NPs modified with G250 in ccRCC tumour tissues was significantly increased, indicating that the nanoplatform could effectively target and accumulate within tumour tissues. Through the combined application of SDT and UTMD, the penetration and accumulation of NPs in tumour tissues were significantly increased, which is crucial for increasing the local drug concentration and enhancing therapeutic effects. After SDT activation, ZnPP successfully generated ROS, which caused significant damage to tumour cells and promoted their death. Additionally, the nanoplatform was equipped with PA, US, and FL imaging capability, enabling both the precise localization of tumours via multimodal imaging technology and real-time monitoring of diagnostic and treatment processes (Scheme 1). In summary, ZnPP@G-PP NPs can significantly increase improve the precision and effectiveness of ccRCC treatment and are safe, and their multimodal imaging capability facilitates the real-time and comprehensive monitoring of the treatment process.

Materials and Methods

Materials

Poly (lactic-co-glycolic acid, lactide: glycolic acid = 50:50, PLGA12, 2000 Da MW) (PLGA-COOH) was synthesized by Shandong Jinan Dagan Biological Engineering Co., Ltd. ZnPP was purchased from J&K Scientific. G250 was purchased from Cell Signaling Technology. Polyvinyl alcohol (PVA, 26.0,0 Da MW), PFP (boiling point of 29°C); 2-(N-morpholino)-ethane-sulfonic acid (MES monohydrate); N-(3-dimethyl-aminopropyl)-N'-ethylcarbodiimide hydrochloride (EDC); N-hydroxysuccinimide (NHS); and the fluorescent dye 1.1-docosine-3,3,3,3-tetramethyltricarbocyanoiodide (DiR), 1.1-octacosalkyl-3,3,3,3-tetramethylindole carbocyanine perchlorate (DiI) and 4.6-diamino-2-phenylindole (DAPI) were purchased from Sigma–Aldrich Co. (Missouri, USA). RPMI-1640 medium, Matrigel, and foetal bovine serum (FBS) were purchased from Gibco Co. (Carlsbad, CA, USA). MitoTracker Deep Red FM was obtained from Invitrogen (Thermo Fisher Scientific), and calxanin AM (CAM), propylene iodide (PI) and Cell Counting Kit-8 (CCK-8) were purchased from Dojindo Molecular Technology (Shanghai, China). Fluorescein isothiocyanate (FITC) conjugated goat anti-human antibodies were purchased from Abcam (Cambridge, UK). 786-O cells and DPSCs were both purchased from Shanghai Zhongqiaoxinzhou Biotech.The other reagents used in this study were analytical grade reagents.

Preparation of ZnPP@ PFP-PLGA NPs

ZnPP@PFP-PLGA NPs (hereafter called ZnPP@PP NPs) were prepared via the double emulsion method, through which ZnPP was loaded on and PFP was encapsulated in PLGA.First, PLGA-COOH (25 mg) dissolved in trichloromethane ($CHCl_3$) (1 mL) and ZnPP (1 mg) dissolved in dimethyl sulfoxide (DMSO) (500 μL) were mixed by oscillation in an ultrasonic cleaner (SB-5200DTDN, New Technology Co., Ltd). to ensure dissolution. Next, PFP (100 μL) was added to the mixture in an ice bath, and the first emulsification step (5 min, 65 w, on; 5 s, off) was performed with an acoustic

vibrometer (XL2020, Heat Systems, Inc., USA) to ensure that the trichloromethane and PFP were evenly mixed. The mixture was poured into a 4% polyvinyl alcohol (PVA) (6 mL) solution and emulsified a second time (5 min, 40 W, on; 5 s, off) to obtain a milky suspension. Isopropyl alcohol (IPA;2%,6 mL) was added to promote volatilization, and the mixture was stirred with a magnetic stirrer (HJ-1, Jiangsu Melting Instrument Company) for 2–4 h. After washing and centrifugation (10,000 r/s, 5 min, centrifuge:5804R;Eppendorf;Hamburg, Germany), ZnPP@PP NPs were obtained and stored at 4°C. In addition, PLGA-PFP NPs (hereafter termed PP NPs) and ZnPP@PLGA NPs (hereafter termed ZnPP@P NPs) were prepared via the same method but with different reagents. DiI/DiR-labeled NPs were fabricated using the same method with the exception of the PLGA and adding 5 μL of DiI/DiR to $CHCl_3$.

G250 Modification

G250 was covalently attached to the shells of the NPs via carbodiimide coupling. First, the ZnPP@PP NPs were resuspended in MES buffer (pH=6). Then, the activators 1-(3-dimethylaminopropyl)-3-ethylcarbodiimide hydrochloride (EDC) and N-hydroxysuccinimide (NHS) were added (molar ratio,PLGA-COOH:EDC:NHS=1:5:15), and the mixture was incubated at low temperature (4°C) for 30–60 min. Next, centrifugation was performed with 2-morpholinoethane-sulfonic acid (MES: pH=6.0) buffer to remove as much of the unreacted activators as possible. The NPs were dissolved by dispersion with MES (pH=8.0) buffer; G250 was then added, and a homogeneous mixture was obtained, and incubated at low temperature for 1–3 h. The target NPs, ZnPP@G250-PFP-PLGA NPs (hereafter termed ZnPP@G-PP NPs), were prepared by three rounds of washing and centrifugation with MES buffer (pH=8.0) to yield in a brown emulsion and were stored at 4°C for later use.

Characterization

Transmission electron microscopy (TEM; Hitachi H-7600, Japan), scanning electron microscopy (SEM; JEOL JEM-7800F) and optical microscopy (OM;CKX41; Olympus, Tokyo, Japan) were used to analyse the morphology, dispersion and particle size distribution of the ZnPP@G-PP NPs. The average particle size, surface potential, and concentration of the NPs were measured with a Malvern particle size analyser and a potentiometer. The absorption spectra and characteristic peaks of the NPs were detected with an ultraviolet spectrophotometer (160-Bio, Thermo Fisher Scientific,USA), and the attachment of G250 was examined via confocal laser scanning microscopy (CLSM;Nikon A1,Tokyo, Japan). The NPs were isolated through ultrafiltration, ultracentrifugation, and dialysis. After the dissolution of free ZnPP, the absorption spectra of the sample were obtained via a UV-Vis spectrophotometer (UV 2550, Shimadzu, Japan). To calculate the encapsulation efficiency(EE) and drug loading capacity (LC) of ZnPP, the absorption spectra of the encapsulated ZnPP were analysed with reference to a standard curve. The standard curve was generated on the basis of the absorption spectra of ZnPP at various concentrations. The EE and LC were calculated via the following formulas: the encapsulation efficiency (%) was calculated as (EE)= (entrapped ZnPP/total ZnPP input) × 100%.The loading capability (%) was calculated as (LC)= (entrapped ZnPP/total weight of NPs) × 100%.

In vitro Phase Transition Experiment

A 3% agarose gel module was prepared and used to incorporate fluorocarbon NPs at various concentrations. These NPs were then exposed to LIFU(2 W/cm^2). The liquid-to-gas phase transition of ZnPP@G-PP NPs during LIFU application was observed via OM,and changes at different time points (0, 1, 3, and 5 min) were recorded to determine the optimal parameters for ultrasonic irradiation.

Detection of ROS Generation

For detection of ROS generated by NPs via the Singlet Oxygen Sensor Green (SOSG) probe,ZnPP@G-PP NPs solutions of different concentrations were prepared, and the SOSG working solution was prepared according to the instructions. These samples were treated with LIFU, and the irradiation time and power were controlled. A fluorescence spectrophotometer was used to determine the fluorescence intensity values, thereby indirectly assessing ROS production.

For measurement of intracellular ROS levels via the 2',7'-dichlorodihydrofluorescein diacetate (DCFH-DA) probe, 786-O cells in the logarithmic growth phase were cultured in confocal dishes to 70–80% confluence, and then

ZnPP@G-PP NPs were then added at different concentrations and incubated for 3 hours. The unphagocytosed NPs were removed by washing with PBS, DCFH-DA solution was added to the cells, and the cells were incubated for 30 min. LIFU was then applied to the cells, and the generation of intracellular ROS was observed via CLSM at different power levels. The production of ROS in 786-O cells in the control group and the experimental groups (LIFU only, ZnPP@G-PP NPs, PP NPs + LIFU, ZnPP@PP NPs + LIFU, ZnPP@G-PP NPs + LIFU) was observed under the same LIFU power.

In vitro Targeting

To evaluate the cellular uptake of NPs, 786-O cells (2×10^5 cells per well) were seeded in a 6-well plate and incubated for 24 h. DiI-labeled NPs were suspended in serum-free RPMI-1640 medium. The culture medium was substituted with the NP samples (ZnPP@PP NPs and ZnPP@G-PP NPs labeled with DiI, 1 mg/mL), incubated for various timepoints (1, 2 and 3 h) and then rinsed with PBS. The cells were digested with pancreatic enzymes and each group of cells were collected. Quantitative analysis was performed using flow cytometry to detect and quantify the fluorescence signal of DiI of cells in various groups, thereby evaluating the uptake amount and efficiency of NPs.

To further confirm the targeting ability of the NPs, we plated 786-O cells (1×10^5 cells per dish) in confocal dishes and allowed them to adhere overnight. Then preprepared NPs were added to dishes containing 786-O cells and incubated for different durations (1, 2, and 3 h). The cells were then washed with PBS four times to remove unbound NPs, and were then fixed with 4% paraformaldehyde (PFA) for 20 min. To demonstrate the targeting specificity of ZnPP@G-PP NPs, we also coincubated ZnPP@G-PP NPs with DPSCs and processed the cells as described above. Finally, the targeted binding of the NPs to the cells and the cellular uptake of NPs were evaluated via CLSM.

In vitro Cytotoxicity Assay

A CCK-8 assay was used to evaluate cell viability and growth. 786-O cells/DPSCs (5×10^3 cells per well) were seeded in 96-well plates and cultured for 24 h. To comprehensively assess the biocompatibility and therapeutic effect of the NPs, we designed three experimental. The experimental groups were as follows. Experimental I: The control group consisted of 786-O/DPSC cells that were not subjected to any treatment. NPs (PP NPs, ZnPP@PP NPs, and ZnPP@G-PP NPs) were resuspended at different concentrations (0.125, 0.25, 0.5, 1 and 2 mg/mL) in culture medium. Then, the medium of each group of cells was replaced with medium containing various nanoparticles and changes in the activity of 786-O cells and DPSC cells were determined after cells cultured for 24 h. Experiment II: For selecting the LIFU power, we divided the experiments into groups as follow: Control (786-O cells), ZnPP@G-PP NPs (0.75 mg/mL), LIFU (1, 2, 3 W/cm^2), ZnPP@G-PP NPs+LIFU (1, 2, 3 W/cm^2). Experiment III: Control (786-O cells without any treatment), LIFU, and 0.25 mg/mL ZnPP@G-PP NPs; different nanoparticles (PP NPs, ZnPP@PP NPs, ZnPP@G-PP NPs) were added at different concentrations (0.25, 0.5 and 0.75 mg/mL) in culture medium. Then, the medium of each group of cells was replaced with medium containing various nanoparticles. After cultured for 3 h, removed the unbound NPs by washing with PBS, the cells in the groups with LIFU were subjected to LIFU intervention (2 W/cm^2, 2 min), and the killing effects of the different concentrations of ZnPP@G-PP NPs on tumour cells under LIFU irradiation were evaluated after cells cultured overnight. In addition, we evaluated the toxicity of ZnPP. In this experiment, 786-O cells in the logarithmic growth phase were incubated with different concentrations of ZnPP (3.125, 6.25, 12.5, 25, 50 and 100 μg/mL) for 24 h to assess the toxicity of ZnPP. In confocal culture dishes, we seeded 786-O cells (10×10^4 cells per well) of the logarithmic growth phase cultured for 24 h. The cells of different groups treated by NPs according to the description for the Experimental Ill, cultured them for 3 h, and then removed the unbound NPs by washing with PBS. After LIFU exposure (2 W/cm2, 2 min), the cells were cultured for another 24 h. Subsequently, the cells were stained with CAM/PI for 30 minutes, and the status of live and dead cells was observed via CLSM. To further elucidate cytotoxicity, we seeded 786-O cells (5×10^5 cells per well, 1 mL) into a 6-well plate and followed the treatment procedure described for Experimental III. After exposure to LIFU (2 W/cm^2, 2 min), apoptosis in the harvested cells was analyzed via FCM.

NPs Penetration Assay

In vitro three-dimensional (3D) cultured tumor spheroids were established. The 786-O cells (5×10^4 cells per well) were seeded per well and cultured for 6 days in spheroid microplates. The cells is divided into two groups: ZnPP@G-PP NPs and ZnPP@G-PP NPs+LIFU. DiI-labelled ZnPP@G-PP NPs were suspended in serum-free RPMI-1640 medium and co-incubated with the cells for 3 h. After incubation, the cells were rinsed with PBS to remove unabsorbed NPs. DAPI was used to label the nuclei, and the CLSM was used to observe the layer-by-layer cellular sections of the tumor cell spheres for 3D reconstruction.

DiI-labelled ZnPP@G-PP NPs (2.0 mg/mL) were added to the prepared gel modules. LIFU (2 W/cm^2, 1 min) was applied to the right side of the gel module, and FL imaging of the gel module was then performed to observe changes in the magnitude and area of fluorescence penetration.

In vitro Visual Imaging

Gel modules were prepared, and various concentrations of ZnPP@G-PP NPs (0.75, 1.0, 1.5, 2.0, 2.5, and 3.0 mg/mL) were added to the gel pores. Imaging was conducted with the PA imaging system (VeVO 2100; FUJIFILM VisualSonics Inc., Canada) at excitation wavelengths ranging from 680 nm to 950 nm. The relative intensities of the PA signals corresponding to different concentrations of ZnPP@G-PP NPs were observed and recorded, and the PA signals at each wavelength were analysed. Scatter plots and regression curves were generated to more clearly demonstrate the relationship between the ZnPP@G-PP NP concentration and the PA signal intensity.

The US imaging capability of the PP NPs and ZnPP@PP NPs was subsequently evaluated with a Mylab90 US diagnostic instrument (Esaote, Italy) equipped with a linear probe (LA523, 12 MHz). US images, including B-mode and contrast-enhanced ultrasound (CEUS) images, were acquired at multiple time points (0, 30, 60, 90, 120, 150 and 180 s).

In vivo Visual Imaging

To establish a small animal tumour xenograft model, 786-O cells were cultured in vitro, and cells in the logarithmic growth phase were collected and subcutaneously inoculated into nude mice to establish the tumour xenograft models. The tumours were then imaged via both PA imaging (VeVO 2100; FUJIFILM VisualSonics Inc., Canada) and US imaging (Mylab90 Ultrasound System,Esaote, Italy).

The tumor-bearing mice were randomly divided into three groups, respectively inject free ZnPP, ZnPP@PP NPs, or ZnPP@G-PP NPs(concentration: 10 mg/kg) by i.v. Based on the results of in vitro PA imaging, the optimal excitation wavelength was determined to be 680 nm. Subsequently, images of the transplanted tumor site were acquired using PA imaging at multiple time points (0, 1, 3, 6, 24, 48 h).

The tumour-bearing mice were again randomly divided into groups (the PP NPs, ZnPP@PP NPs, and ZnPP@G-PP NPs groups), and all mice received tail vein injections of ZnPP@G-PP NPs (10 mg/kg). LIFU was applied to the tumour sites, and B-mode and CEUS images of the xenograft tumours were acquired before LIFU exposure and 6 hours after LIFU exposure.

In vivo Targeting

Tumour-bearing mice were administered DiR-labelled ZnPP@G-PP NPs (10 mg/kg) via the tail vein. FL imaging was conducted with a fluorescence imaging system (Fx7 IR Spectra, VilberLourmat, France) at specific time points (0, 1, 2, 4, 6, 24 and 48 h). After 48 h, the tumour-bearing mice were sacrificed, and fluorescence imaging of major organs (heart, liver, spleen, lung, and kidney) and tumours was performed to understand the distribution and metabolism of the NPs in vivo and to better understand their role in tumour biodistribution.

In vivo Biosafety Experiment

Thirty healthy BALB/c mice were randomly divided into 6 groups with 5 mice in each group. The mice in the control group were injected with saline (200 μL), whereas the mice in the other groups were injected with of ZnPP@G-PP NPs (100 mg/kg). The mice were sacrificed at different time points (0, 1, 3, 7, 15, and 30 d), and blood was collected via

retro-orbital bleeding for routine blood tests and biochemical analysis. Moreover, haematoxylin and eosin staining was performed on major organs (heart, liver, spleen, lung, and kidney) for histopathological analysis.

In vivo Synergistic Tumor Therapy

The tumour-bearing mice were randomly divided into 6 groups: the control, LIFU only, ZnPP@G-PP NPs, PP NPs +LIFU, ZnPP@PP NPs+LIFU, and ZnPP@G-PP NPs+LIFU groups. Every 3 days, saline (control, 200 μL) or NPs (10 mg/kg) were injected via the tail vein. Six hours after each injection, the mice were anaesthetized, and the tumour area was treated with LIFU (3 W/cm^2, 5 min) once daily for five consecutive days. Body weight and tumour volume were measured every other day during the treatment period. On the 21st day after the final treatment, the mice were sacrificed, and the tumours were weighed. The longitudinal diameter (a) and transverse diameter (b) of each tumours were measured daily with callipers to calculate the tumour volume (V) with the following equation:

$$V\left(mm^3\right) = ab^2/2$$

Histological and Immunohistochemical Analyses

Two days after the mice were sacrificed, histological and immunohistochemical analyses were conducted on the organs and tumours. The methods included and H&E staining, proliferating cell nuclear antigen (PCNA) staining, and terminal deoxynucleotidyl transferase dUTP nick end labelling (TUNEL). CLSM) was used to visualize the tissue sections, analyse cellular apoptosis and proliferation, and obtain more specific information on cell structure and function.

Statistical Analysis

Statistical analysis was conducted via one-way analysis of variance (ANOVA), two-way ANOVA,or three-way ANOVA. The data are presented as the means ± standard deviations (SDs), with P values indicating statistical significance as follows: $*P < 0.05$, $**P < 0.01$, and $***P < 0.001$.

Results and Discussion

Characterization of the NPs

ZnPP@G-PP NPs were synthesized via a double emulsion method and carbodiimide coupling.[37–39] The SEM images revealed that the ZnPP@G-PP NPs had a well-defined spherical structure with a uniform size and diffuse distribution (Figure 1A). The TEM images further confirmed the spherical structure of the NPs and their potential core–shell architecture (Figure 1B). In the OM images, the NPs displayed a punctate distribution with a uniform spherical morphology (Figure 1C).A Malvern particle size analyser was used to measure the particle size and zeta potential of the PP NPs, ZnPP@PP NPs, and ZnPP@G-PP NPs,which were 213.9±0.173 nm, 248.0±0.100 nm, and 286.9±0.096 nm, respectively (Figure 1D). Concurrently, as the composition of the NPs changed, their zeta potential also changed, with values of −14.33±0.55 mV, −18.47±0.61 mV, and −23.27±1.15 mV for the PP NPs, ZnPP@PP NPs, and ZnPP@G-PP NPs, respectively (Figure 1E). The increase in particle size and change in charge indirectly prove the successful encapsulation of ZnPP and the successful loading of G250. A negative zeta potential ensures that NPs do not aggregate, thereby maintaining their uniform distribution in solution and increasing their stability.[40] The imperfect structure of new tumour blood vessel walls allows the penetration of NPs with diameters less than 700 nm.[41] Our constructed ZnPP@G-PP NPs had a relatively uniform diameter, which allowed them to freely extravasate from tumour blood vessels into tumour tissue, thus reducing damage to normal tissues and cells. In other words, this carrier helps to improve therapeutic effects while reducing damage to surrounding tissues.[9]

The ZnPP@G-PP NPs formed a uniform brownish emulsion, whereas the PP NPs formed a uniform milky white emulsion, with no significant stratification observed after standing (Figure 1F),these results indicated that the prepared NPs had definite stability and dispersibility. As shown in Figure 1G, ZnPP displays two characteristic peaks in the UV absorption spectrum, which are located at approximately 549 nm and 586 nm. The PP NPs without encapsulated ZnPP did not exhibit these two characteristic peaks, whereas ZnPP@PP NPs and ZnPP@G-PP NPs that had successfully

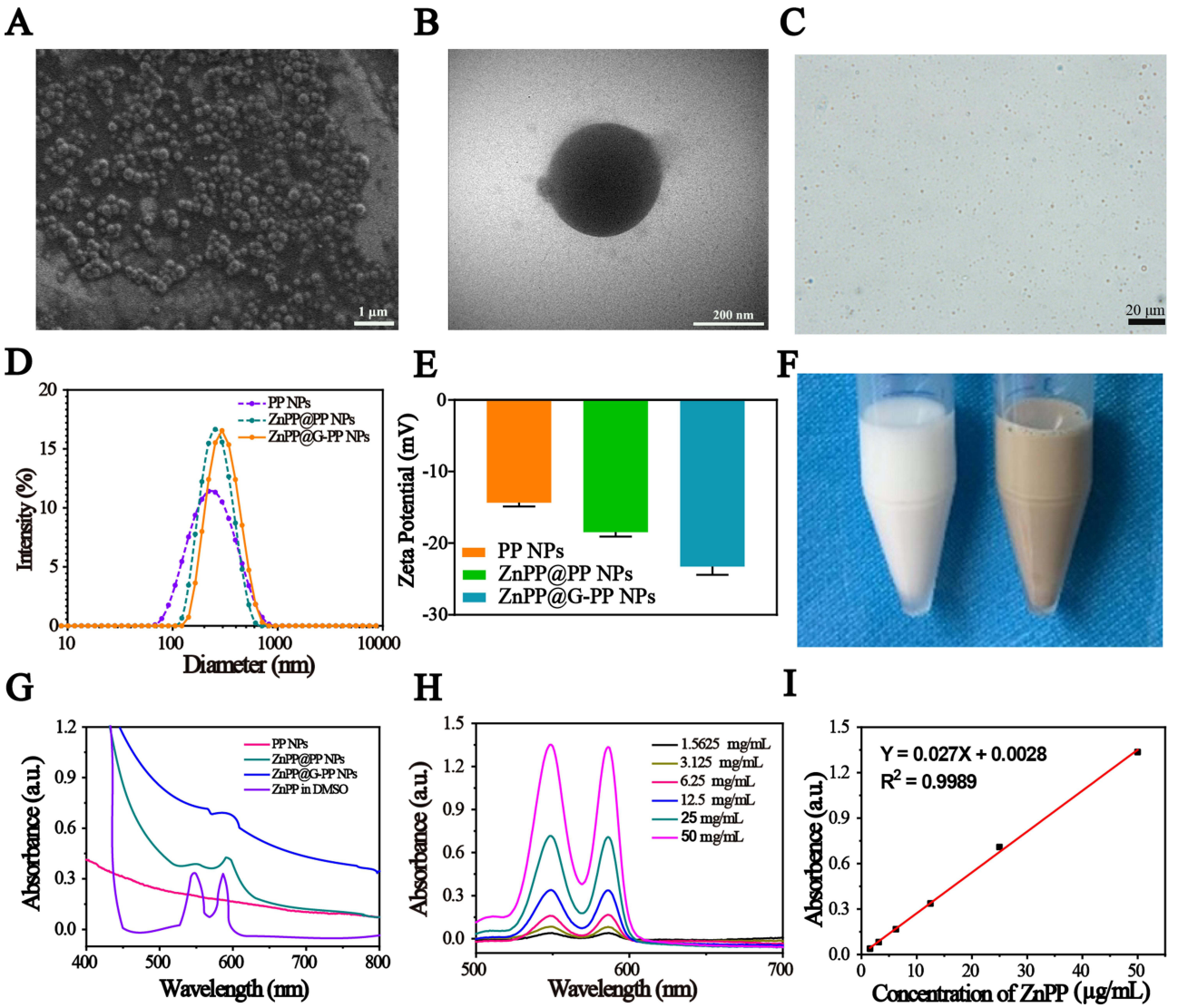

Figure 1 The morphology and characteristics of the ZnPP@G-PP NPs. (**A**) SEM image and (**B**) TEM image of ZnPP@G-PP NPs. (**C**) OM image of ZnPP@G-PP NPs. The scale bar indicates 20 μm. (**D**) Size distribution and (**E**) zeta potential values of NPs (PP NPs, ZnPP@PP NPs, and ZnPP@G-PP NPs). (**F**) Appearances of PP NP (left) and ZnPP@G-PP NP (right) nanoemulsions. (**G**) UV-Vis absorption spectra of PP NPs, ZnPP@PP NPs,ZnPP@G-PP NPs,and free ZnPP in DMSO. (**H**) Ultraviolet absorption spectra of ZnPP at different concentrations in DMSO. (**I**) The corresponding concentration–absorption intensity relationship at a wavelength of 586 nm.

encapsulated ZnPP exhibited the unique UV absorption peaks of ZnPP, proving the successful encapsulation of ZnPP. Moreover, different concentrations of ZnPP in DMSO exhibited these two characteristic peaks in the UV absorption spectra (Figure 1H), indicating the reliable presence of ZnPP. On the basis of the UV absorption curve, we plotted a standard curve of the absorbance of ZnPP against its concentration at a wavelength of 586 nm (Figure 1I), and we determined that the EE of ZnPP in the ZnPP@G-PP NPs was 93.25%, with a drug loading rate of 3.59%. CLSM revealed that FITC-labelled G250 (green fluorescence) successfully combined with DiI-labelled ZnPP@PP NPs (red fluorescence) to form ZnPP@G-PP NPs (yellow fluorescence) (Figure 2A), further verifying the effective interaction between G250 and ZnPP@PP NPs.

In vitro Phase Transition Experiment

After LIFU exposure, the ZnPP@G-PP NPs exhibited unique phase transition characteristics. OM images acquired at different irradiation times revealed that, as the irradiation time increased, these NPs gradually transitioned from a microsphere state to a MBs state (Figure 2B). At an irradiation time of 1 min, only a few NPs had begun this phase

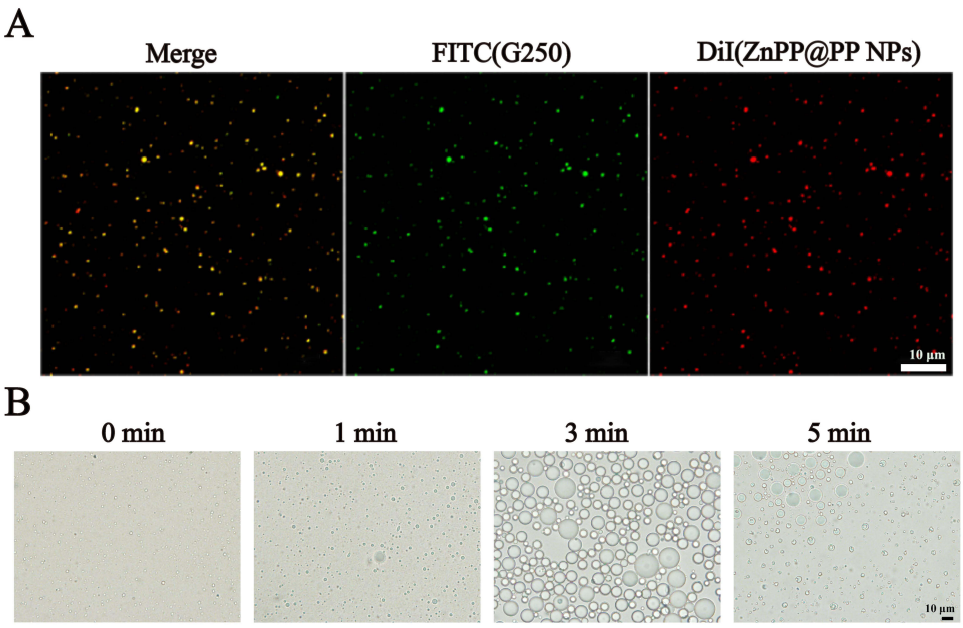

Figure 2 (**A**) The CLSM images of FITC-labelled G250 on the surface of DiI-labelled ZnPP@PP NPs. The scale bar indicates 10 μm. (**B**) Phase change experiment in vitro. Light microscopy images of the LIFU-irradiated ZnPP@G-PP NPs at different times. The scale bar indicates 10 μm.

transition; by 3 min, most of the NPs were in a phase transition state; and when the irradiation time was further extended to 5 min, most NPs not only had undergone the phase transition but also had fragmented into MBs. This phase transition and fragmentation phenomenon occurred because the internal PFP of the NPs reached the phase transition temperature. This structural transition indicates that by adjusting the time and intensity of LIFU irradiation, the degree of phase transition of the NPs, and even their fragmentation into MBs, can be precisely controlled. Such precise control is important for the highly selective delivery of drugs to tumour cells.[42] This ability not only increases the therapeutic effect but also provides a solid theoretical and experimental foundation for the multimodal imaging capability of ZnPP@G-PP NPs and their therapeutic use.[43] Through the induction of this process, we can deliver drugs to tumour cells more controllably, accurately, and effectively for achieving precision therapy.[44]

Detection of ROS Generation

Under LIFU exposure, as the duration and intensity of irradiation increase, the amount of ROS produced by the ZnPP@G-PP NPs also increased accordingly (Figure 3A and B). Additionally, with increasing irradiation power, the production of ROS in 786-O cells observed via CLSM increased (Figure 3C). At the same irradiation power, the effect of ZnPP@G-PP NPs + LIFU on ROS production was significantly greater than that of the other treatments (Figure 3D). These results reveal that by adjusting the irradiation time and intensity of LIFU, the generation of ROS can be effectively controlled, allowing precise control over the production of ROS. Thus, the administration of NPs in combination with LIFU exposure can further increase the production of ROS, showing potential for improved therapeutic effects and constituting a promising method for tumor treatment.

In vitro Targeting

The key factors for ensuring the precise diagnostic capability and sonodynamic therapeutic effects of a nanoplatform include its specificity and ability to regulate its effective accumulation.

The uptake of NPs (ZnPP@PP NPs or ZnPP@G-PP NPs) by 786-O cells was evaluated at different timepoints (1, 2, and 3 h) via FCM (Figure 4A). The cellular uptake of the ZnPP@G-PP NPs at 2 h was significantly greater than that of the ZnPP@PP NPs (80.17% vs 34.28%). At 3 h, phagocytic saturation was essentially reached; although the uptake continued to increase, the difference between the groups was not significant, and this phenomenon might be related to

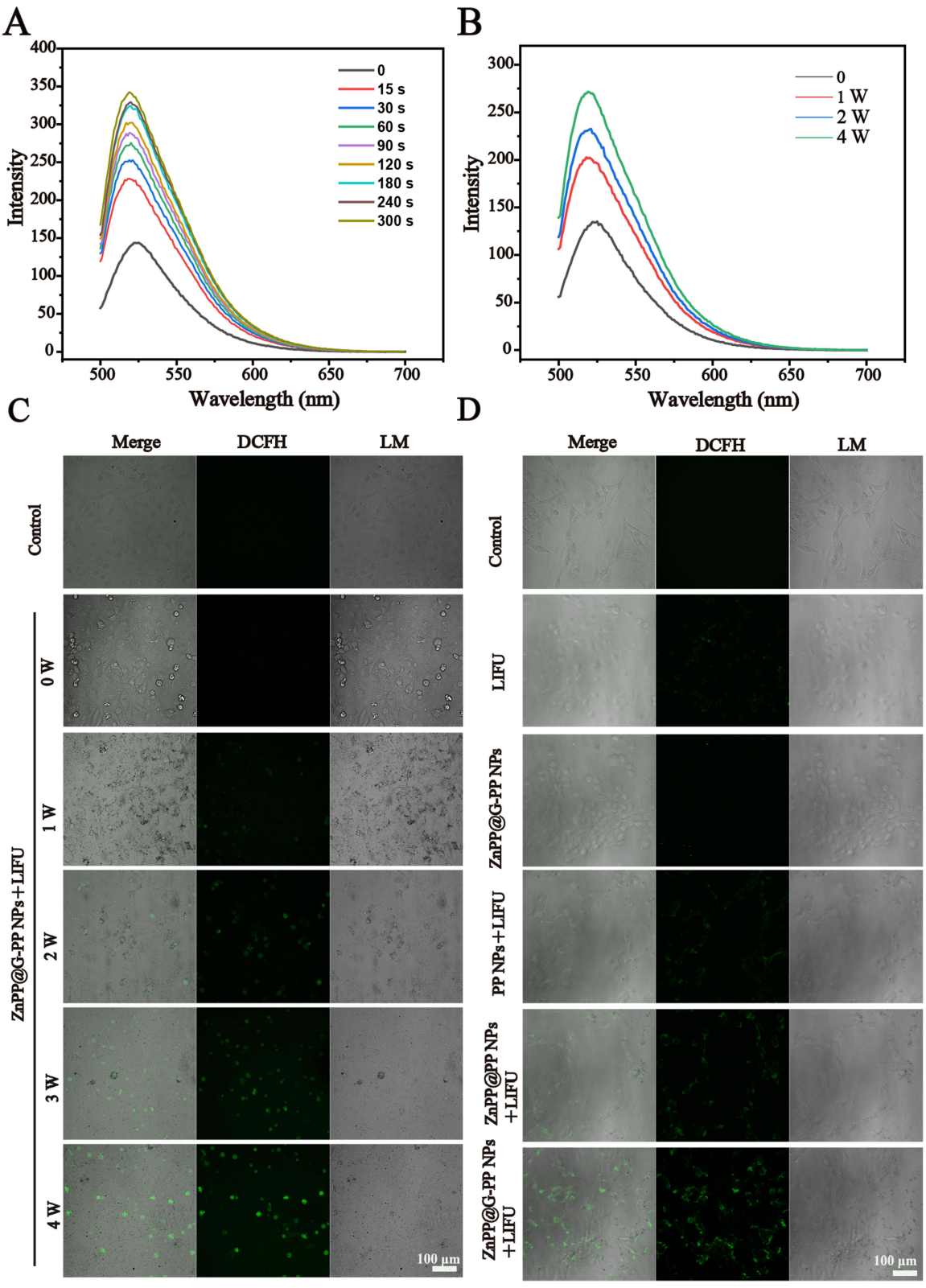

Figure 3 ROS production by ZnPP@G-PP NPs (**A**) ZnPP@G-PP NPs after LIFU irradiation for varying durations. (**B**) ROS production by ZnPP@G-PP NPs following LIFU irradiation at different power levels. (**C**) CLSM images of ROS production in 786-O cells in the control group and experimental group (ZnPP@G-PP NPs) after LIFU irradiation at different power levels. The scale bar indicates 100 μm. (**D**) CLSM images of ROS production in 786-O cells in the control group and experimental groups (LIFU, ZnPP@G-PP NPs, PP NPs+LIFU, ZnPP@PP NPs+LIFU, and ZnPP@G-PP NPs+LIFU). The scale bar indicates 100 μm.

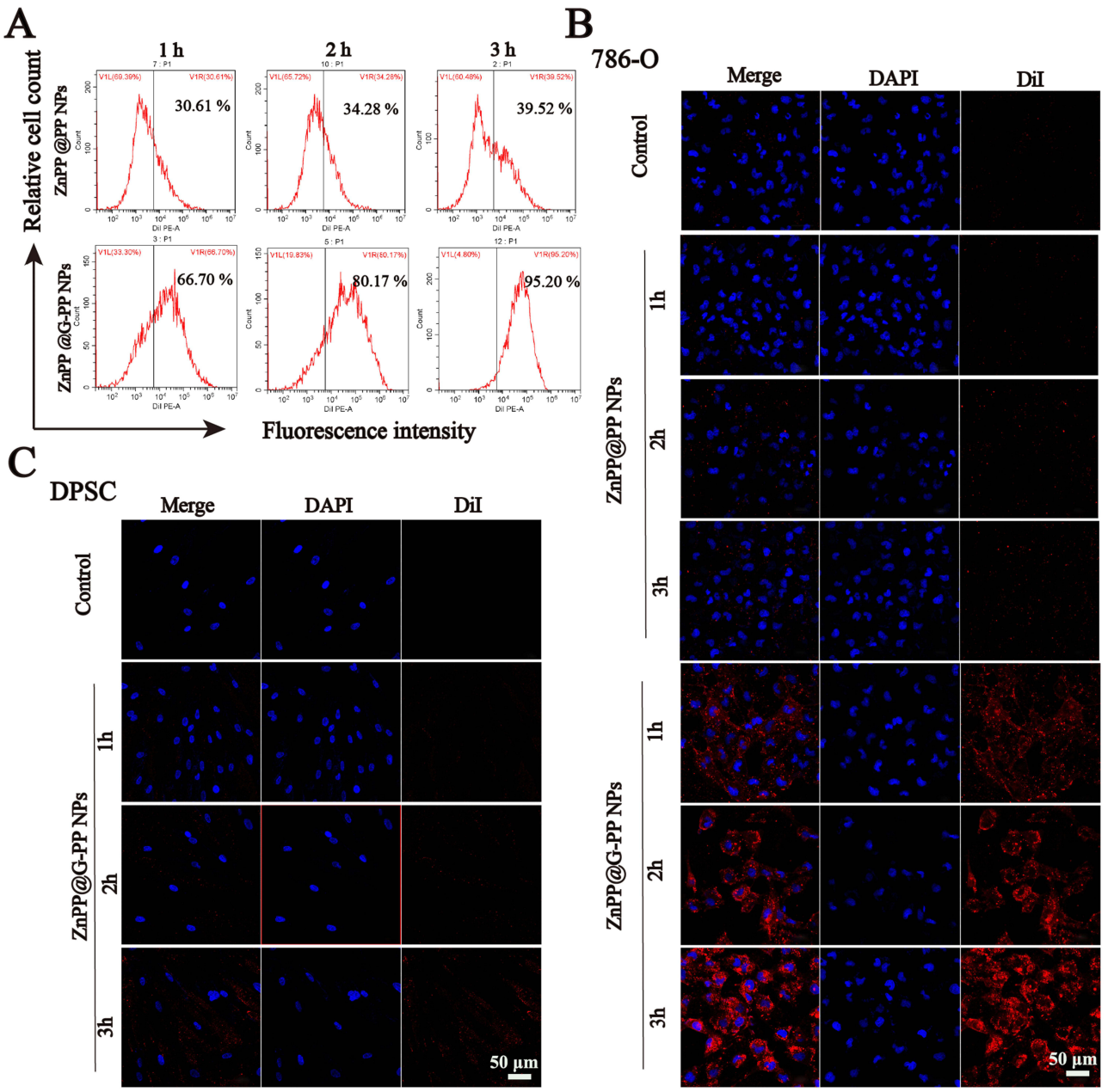

Figure 4 In vitro targeting. (**A**) Quantitative analysis of the cellular uptake behavior of NPs (ZnPP@PP NPs, and ZnPP@G-PP NPs) after different intervals of incubation analysed by FCM. (**B**) CLSM images of 786-O cells inclubated with the control group (first row), ZnPP@PP NPs for 1,2,3 hours (second to fourth rows), and ZnPP@G-PP NPs for 1,2,3 hours (fifth to seventh rows). From right to left: DiI-labelled NPs, DAPI-labelled nuclei and the corresponding merged images. The scale bar indicates 50 μm. (**C**) CLSM images of DPSC cells inclubated with the control group (first row), ZnPP@G-PP NPs for 1, 2, 3 hours (second to fourth rows). From right to left: DiI-labelled NPs, DAPI-labelled nuclei and the corresponding merged images. The scale bar indicates 50 μm.

cellular endocytosis. These results indicate that the phagocytosis of targeted NPs become more efficient over time, whereas nontargeted NPs undergo general phagocytosis, with only a slight increase in efficiency over time. In addition, these results confirmed that G250 targeted 786-O cells, allowing efficient accumulation of NPs within these cells and providing strong evidence for their suitability for targeted therapy of RCC.

To further verify the targeting ability of G250, NPs were labelled with DiI, and the targeted binding and cellular uptake of these NPs were observed via CLSM. In 786-O cells, the fluorescence signal of the ZnPP@G-PP NPs was significantly stronger than that of the ZnPP@PP NPs and the control. With increasing incubation time, the red fluorescence signal in the perinuclear region of 786-O cells gradually increased in the ZnPP@G-PP NPs group, while

almost no red fluorescence signal was detected in the control group or the ZnPP@PP NPs group (Figure 4B).Compared with that in DPSCs that did not express G250, the fluorescence in DPSCs that were treated with ZnPP@G-PP NPs was very weak (Figure 4C). These findings further proved that ZnPP@G-PP NPs can specifically target 786-O cells that express G250. Therefore, G250 is as an ideal target for the diagnosis and treatment of ccRCC[45–47] because it facilitates highly efficient specificity and selectivity through active targeting, enabling the precise localization of NPs to precisely localize to and effectively accumulate in tumour tissues, resulting in improved therapeutic effects and reduced side effects.

In vitro Cytotoxicity

The effects of different concentrations of NPs (PP NPs, ZnPP@PP NPs, and ZnPP@G-PP NPs) on the viability of 786-O cells were evaluated via a CCK-8 assay, and differences were observed (Figure 5A). PP NPs were previously found to be nontoxic at all concentrations tested, indicating their good biosafety as drug carriers.[48,49] At concentrations less than 1 mg/mL, NPs encapsulating ZnPP (ZnPP@PP NPs and ZnPP@G-PP NPs) had a minimal effect on cell viability (with a viability rate above 80% in both groups). However, when the NP concentration exceeded 1 mg/mL, slight toxicity was observed. These NPs had off-target effects on noncancer cells (DPSCs) (Figure 5B), indicating that they do not damage healthy tissues. In the ZnPP drug toxicity assay (Figure 5C), ZnPP itself exhibited a certain degree of cytotoxicity; when the cells were incubated with 3.125 μg/mL ZnPP, the cell survival rate was 55.86%, and significant cytotoxicity of ZnPP was observed for concentrations above 12.5 μg/mL. However, when ZnPP was encapsulated in PLGA to form NPs, the toxicity of ZnPP was significantly reduced. These findings indicate that the use of appropriate drug carriers or controlled release systems can significantly improve the biosafety of drugs. In the therapeutic effects of LIFU combined with ZnPP@G-PP NPs at different powers on cells, we found that ZnPP@G-PP NPs had excellent therapeutic effects on tumor cells at LIFU power of 2 W/cm² and 3 W/cm², but there was little difference between the two groups (Figure S3). We selected the power of 2 W/cm^2 for in vitro experiments, as the fact that the power of 3 W/cm^2 will change the cell from the adhesion state to the suspension state, and make cell collection difficult, affecting analysis and detection, and using a lower power helps avoid this difficulty. When PP NPs, ZnPP@PP NPs, or ZnPP@G-PP NPs were used in combination with LIFU, dose-dependent cytotoxicity was observed (Figure 5D). Notably, the ZnPP@G-PP NPs+LIFU group exhibited stronger cytotoxicity than the ZnPP@PP NPs+LIFU group did, further confirming that the administration of targeted NPs combined with LIFU can significantly increase the extent of cell death. Observation of the killing effect on 786-O cells under different treatment conditions via CLSM (Figure 5E) revealed that ZnPP@G-PP NPs+LIFU had the most significant killing effect on cells, with an apoptosis rate of 100%. The killing effect of LIFU was limited, but its combination with NPs significantly increased the cell killing effect. This finding is similar to the results that were observed by FCM (Figure 5F), where the proportion of apoptotic cells in the ZnPP@G-PP NPs +LIFU group was the highest, far exceeding that in the other groups. The results of this study provide new ideas and strategies for the combined application of nanomedicine and physical therapeutic modalities. By optimizing drug carriers and combining sonosensitizers with physical therapeutic modalities, more efficient and less toxic tumour treatment methods can be developed.

NPs Penetration Assay

The 3D tumour spheroid penetration assay is a crucial method for assessing the ability of NPs to penetrate into tumour region. In this experiment (Figure 6A and 6B), we observed that NPs was only ingested on the surface of 3D tumour spheroids in the control group, while NPs was ingested at the depth of 3D tumour spheroids in the ZnPP@G-PP NPs +LIFU group. The results showed that a certain barrier on the surface of 3D tumour spheroids prevented the deep penetration of NPs, and LIFU combined with NPs was able to break through this barrier, allowing NPs to enter the depth of the 3D tumor ball and be taken up by cells. The penetration depth of ZnPP@G-PP NPs in complex tumour microenvironments is limited, using LIFU to break this barrier could significantly enhance the penetration of NPs, which should be the critical role of SDT and UTMD.[50,51] Thereby increasing drug permeability and efficacy. This discovery provides a new strategy for improving drug delivery efficiency and therapeutic outcomes in tumour tissues.[52,53]

To further understand the mechanism by which LIFU regulates cell membrane permeability, we conducted an in vitro NPs penetration assay via FL imaging (Figure 6C). The results showed that as the distance increased, the magnitude and

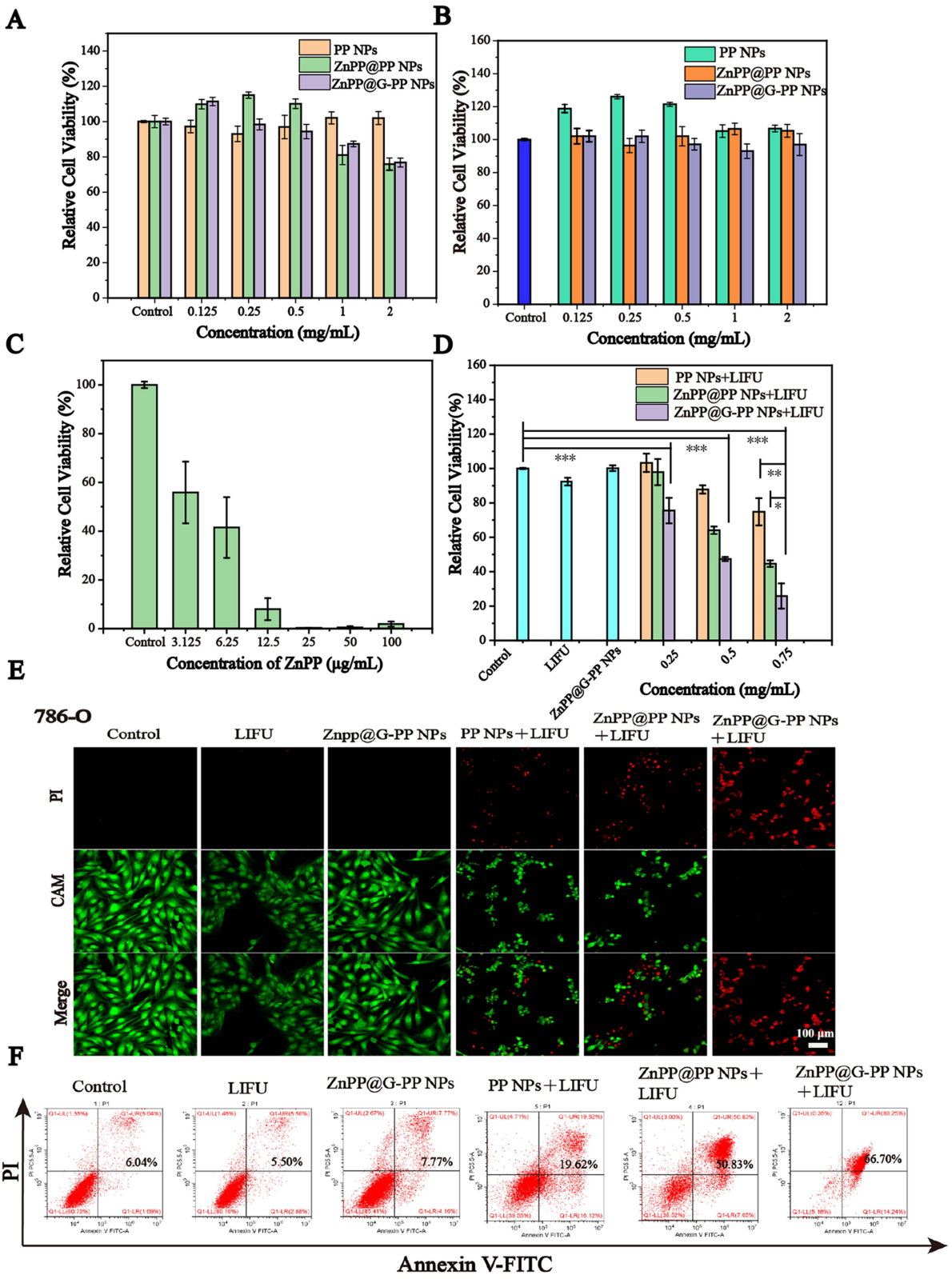

Figure 5 In vitro cytotoxicity. Relative viability of (**A**) 786-O cells and (**B**) DPSC cells after incubation with various concentrations of NPs (PP NPs, ZnPP@PP NPs, ZnPP@G-PP NPs). (**C**) Drug toxicity tests of ZnPP. (**D**) Viability of 786-O cells after incubation with different treatments, Control,LIFU, ZnPP@G-PP NPs, and various concentrations of distinct nanoparticles (PP NPs, ZnPP@PP NPs, ZnPP@G-PP NPs) under LIFU intervention. (**E**) CLSM images of 786-O cells subjected to different treatments (Control, LIFU, ZnPP@G-PP NPs, PP NPs+LIFU, ZnPP@PP NPs+LIFU, and ZnPP@G-PP NPs+LIFU) and stained with CAM and PI. CAM-labelled live cells and PI-labelled dead cells. The scale bar indicates 100 μm. (**F**) FCM analysis of cell apoptosis after administering different treatments.(n=3, **P* < 0.05, ***P* < 0.01, ****P* < 0.001).

https://doi.org/10.2147/IJN.S459960 DovePress

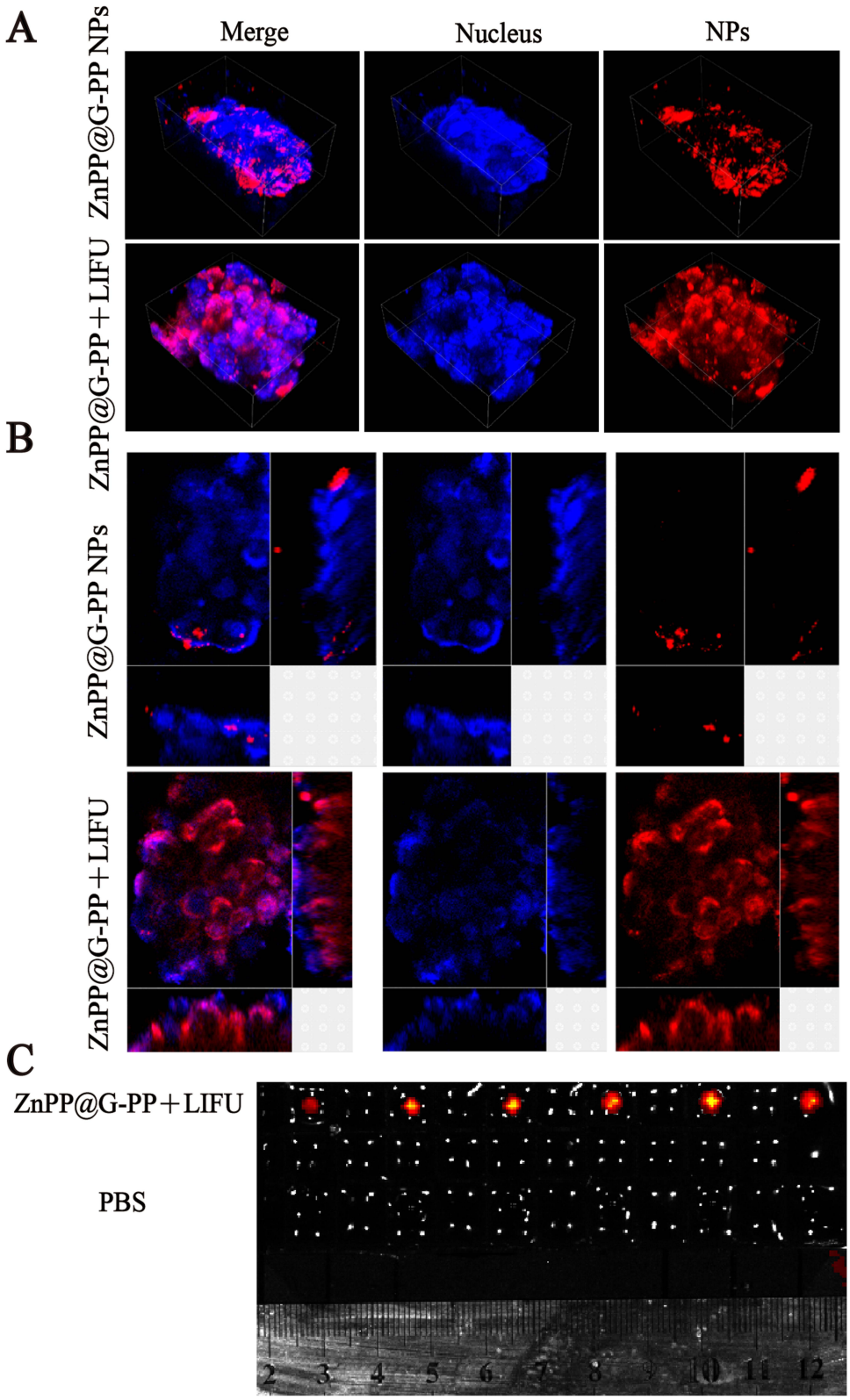

Figure 6 (**A**) Reconstruction of the permeability of 3D tumour cell spheres to ZnPP@G-PP NPs and ZnPP@G-PP NPs+LIFU and (**B**) three-angle imaging. (**C**) Fluorescence imaging experiment of NPs penetration in vitro. Penetration of ZnPP@G-PP NPs at different distances in the gel model after LIFU irradiation on the right side.

area of NPs penetration also decreased. This finding indicates that the impact of LIFU on NPs penetration is closely related to the irradiation distance. When the US focus is close to the gel model orifice, the effect of LIFU on NPs penetration is most significant; however, the influence of US gradually diminished with increasing distance. Therefore, the effectiveness of LIFU treatment for tumours is closely related to the tumour depth.[22,54,55]

In summary, through in vitro penetration assays, we were able to observe the distribution and penetration of NPs within tumour spheroids and evaluate the impact of LIFU on NPs penetration ability. These data provide valuable information for designing clinical treatment, helping us to better understand and apply LIFU to increase the efficacy of tumour therapy.

In vitro Imaging and Evaluation of Targeting Performance

PA is a cutting-edge imaging technique that has attracted attention because of its exceptional precision. In our experiments, we selected 680 nm as the PA excitation wavelength and observed the PA signals of the ZnPP@G-PP NPs (Figure 7A). As the concentration of ZnPP@G-PP NPs increased (0.75–3.0 mg/mL), the PA signals increased linearly. The PA signal values increased from 0.342 to 1.929, and the relative PA signal values in the corresponding region of interest ROI also increased significantly. PA salines were not produce in the saline control group under the same experimental conditions, further confirming proving the superiority of ZnPP@G-PP NPs in PA imaging. This discovery lays a foundation for the diagnostic of ZnPP@G-PP NPs.

ZnPP@G-PP NPs demonstrate exceptional acoustic droplet vaporization properties, creating ideal conditions for US imaging. In this experiment, we monitored changes in US images (B-mode and CEUS) of PP NPs and ZnPP@G-PP NPs at various time points (0, 30, 60, 90, 120, 150, and 180 s). As the irradiation duration increased, a signal peaked around 2 minutes followed by a gradual decline (Figure 7B). Compared to the control group, the ZnPP@G-PP NP group exhibited significant advantages in US imaging, as the ZnPP@G-PP NPs were able to depict the ROI more distinctly, thereby elevating the precision and dependability of diagnostics. Both ZnPP@PP@G-PP NPs and PP NPs contain PFP, yet they exhibit notable differences in vitro US imaging effects, with ZnPP@PP@G-PP NPs showing enhanced performance in vitro US imaging. This discrepancy can be ascribed to the incorporation of ZnPP, serving as a porphyrin-based sonosensitizer, which markedly amplifies the UTMD effect. By augmenting the generation and oscillation strength of microbubbles, ZnPP improves the phase transition efficiency, facilitating the transition of the phase change material from a liquid to a gaseous state under LIFU. Such transformation optimizes the quality of US imaging and enhances therapeutic outcomes.[56] In summary, ZnPP@G-PP NPs boast notable advantages in both PA/US imaging and targeting, offering innovative tools and methodologies for medical diagnosis and therapy, and hold broad potential applications.

In vivo Imaging and Evaluation of Targeting Performance

On the basis of the in vitro PA/US imaging capabilities of the ZnPP@G-PP NPs, we analysed the multimodal imaging capability in 786-O tumour-bearing mice in vivo. The key factors for tumour imaging are the initial time and the cycle time, which depend mainly on the ability for effective accumulation of NPs within tumour cells.[57] PA imaging was performed by acquiring images and quantitatively analysing the tumour area within 0–48 h after intravenous injection of ZnPP@G-PP NPs. The results showed that the ZnPP@G-PP NPs exhibited significant advantages in tumour imaging. A faint signal appeared at 1 h postinjection, rapidly increased to a peak within 6 h, began to decrease after 24 h, and showed a weakening trend until 48 h. However, in the ZnPP@PP group, weak signals were observed at 1 h postinjection and peaked at 24 h, and the signal intensity was much poorer than that in the ZnPP@G-PP NPs group during the whole imaging process. In contrast, the control group ZnPP NPs showed no significant changes during the same period (Figure 7C). ZnPP@G-PP NPs have strong targeting and bioaccumulation abilities while also allowing the monitoring of NP distribution and aggregation in the tumour area via PA signal strength.

For in vivo US imaging, an optimal PA imaging time of 6 h was used, and NPs (PP NPs, ZnPP@PP NPs, and ZnPP@G-PP NPs) were intravenously injected into the mice, followed by LIFU irradiation to obtain US images of the tumour area (Figure 7D). The experimental results revealed that there were no significant changes in the B-mode or CEUS before or after LIFU irradiation in either the PP NP or the ZnPP@PP NP groups, whereas a significant difference was observed before and after LIFU irradiation in the ZnPP@G-PP NP group. This confirmed that the NPs loaded with

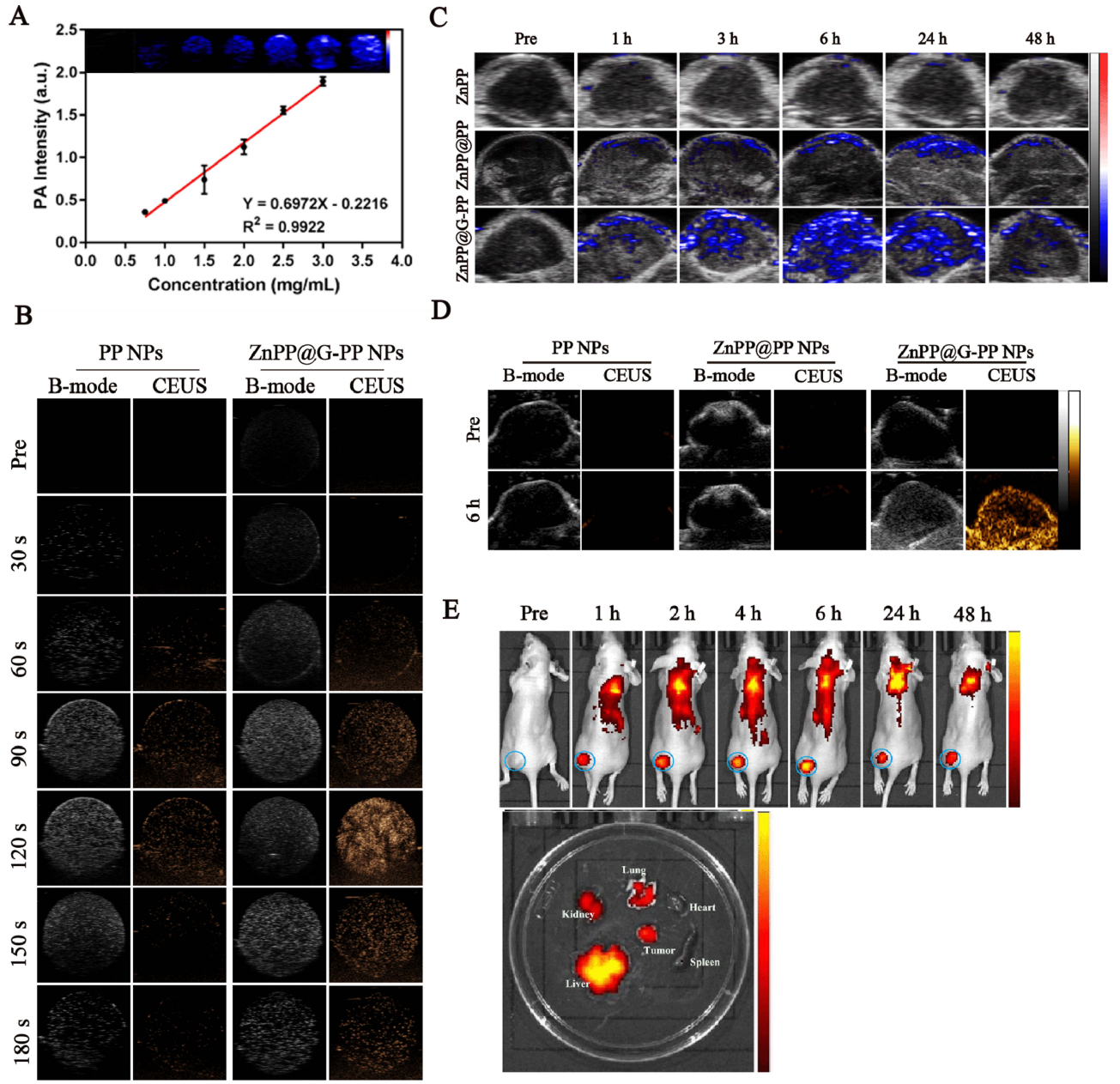

Figure 7 PA/US imaging (**A**) Quantitative analysis of the relationship between the ZnPP@G-PP NP concentration and PA signal intensity (n=3). Inset: corresponding PA images of ZnPP@G-PP NPs at elevated concentrations. (**B**) Ultrasonic images of PP NPs and ZnPP@G-PP NPs after LIFU irradiation for different durations. (**C**) PA images of tumours after intravenous injection of NPs (free ZnPP, ZnPP@PP NPs, ZnPP@G-PP NPs). (**D**) US imaging of tumours at 6 h postinjection of NPs (PP NPs, ZnPP@PP NPs, ZnPP@G-PP NPs) before and after irradiation. (**E**) Biodistribution of the ZnPP@G-PP NPs. In vivo FL imaging of BALB/c nude mice at different time points after intravenous injection of DIR-labelled ZnPP@G-PP NPs and in vitro FL imaging of tumours and vital organs 48 h after intravenous injection.

PFP underwent a liquid–to–gas phase transition in the tumour area upon LIFU irradiation, laying the foundation for imaging. NPs with targeting capabilities can accumulate within tumours in a short time and remain stable In vivo PA/US imaging confirmed that the ZnPP@G-PP NPs exhibited excellent targeting capabilities and efficiently accumulated at the tumour site in a relatively short time. Furthermore, PA/US imaging could be used to monitor the distribution and accumulation of NPs in the tumour area in real time, providing important guidance for tumour diagnosis, treatment, and prognosis assessment.

Additionally, FL imaging technology was used to evaluate the tumour biodistribution of the ZnPP@G-PP NPs in 786-O tumour-bearing mice (Figure 7E). Strong fluorescence signals consistently concentrated in the tumour area, peaking at 6 h. The

ex vivo FL images were analyzed at 48 h postinjection indicated that tumour and major organs (liver, kidneys, and lungs) still revealed FL signal intensity. It is possible that nanoparticles are primarily metabolized by major organs. The distribution of ZnPP@G-PP NPs in vivo indicated that strong FL signals were concentrated in the tumour area, suggesting that ZnPP@G-PP NPs possess good targeting capability and accumulate rapidly within tumours, which were sustained and stable, demonstrating great potential in tumour therapy.

In vivo Biocompatibility Evaluation

A comprehensive biochemical analysis and histological assessment were conducted on BALB/c mice after tail vein injection of ZnPP@G-PP NPs to evaluate the in vivo biosafety of these NPs. At multiple time points (0, 1, 3, 7, 15, and 30 d), there were no significant changes in complete blood counts, liver function test results, renal function test results, or cardiac enzyme levels in the mice that were injected with ZnPP@G-PP NPs (Figure S1). These findings indicate that ZnPP@G-PP NPs do not have significant toxic effects on organs such as the liver or kidneys or affect the haematological system or other vital physiological functions. Additionally, pathological changes in the major organs of the mice were assessed via H&E staining (Figure S2), and no obvious acute or chronic histological alterations were observed. These findings suggest that the ZnPP@G-PP NPs exhibit good biocompatibility and safety in vivo, which not only helps to reduce potential off-target effects and damage to surrounding tissues but also provides strong support for the clinical translation of the ZnPP@G-PP NPs.

In vivo Synergistic Tumour Therapy

Based on the ideal in vivo targeting ability exhibited by ZnPP@G-PP NPs, the therapeutic efficacy of anti-tumor treatment was monitored in 786-O tumor-bearing mice. Different treatment regimens were administered to groups of mice, and tumor growth was observed over 21 days. The therapeutic effect was assessed by measuring changes in tumor volume (Figure 8A). Additionally, photographs of all mice were recorded (Figure 8B) to more intuitively demonstrate the therapeutic effects. Compared with those in the control group, the tumour volume in the LIFU-only group were not significantly lower, indicating that the treatment effect without NPs was not significant. The treatments with untargeted NPs, namely, ZnPP@G-PP NPs, PP NPs+LIFU, and ZnPP@PP NPs+LIFU, were also less effective, possibly due to insufficient accumulation of the NPs in tumour cells. ZnPP@G-PP NPs+LIFU, however, achieved a marked therapeutic effect, which proves that the combination of NPs and LIFU can increase the accumulation of NPs in the tumour area to achieve more effective treatment. Notably, even without the assistance of LIFU, ZnPP@G-PP NPs still demonstrated anti-tumor activity, primarily due to the action of the G250 antibody. Since G250 can specifically bind to this plasma membrane protein, triggering an antigen-antibody reaction that activates the body's immune system to attack the tumor, it may produce therapeutic effects.[58,59] However, the inability of in vitro experiments to fully replicate the complex environment of the in vivo immune system may be a major reason for the differences in results between in vitro and in vivo experiments.[60] Therefore, ZnPP@G-PP NPs+LIFU group significant therapeutic effect strongly proved that the combination of efficient accumulation of NPs and LIFU can achieving better therapeutic effects.

To gain a deeper understanding of the in vivo synergistic anti-tumor effects of ZnPP@G-PP NPs under LIFU irradiation, we performed immunohistological examinations on tumor tissues. H&E staining results showed significantly more necrosis and apoptosis in the ZnPP@G-PP NPs+LIFU group. PCNA staining and the TUNEL assay revealed the presence of representative proliferating cells (red fluorescence) and apoptosis positive cells (green fluorescence) in each group, consistent with the H&E staining results (Figure 9). Additionally, Figure S4 demonstrates that observing the H&E stained slices of major organs from each treatment group showed no adverse reactions in all mice organs, indicating that the treatment methods are safe and reliable.

ZnPP@G-PP NPs are a multifunctional diagnostic and therapeutic platform with a core-shell spherical structure. Through SDT and UTMD effect, this platform can efficiently and precisely deliver drugs to tumor cells and enable personalized diagnosis and treatment under the guidance of multimodal imaging. Compared to existing nanotechnologies, ZnPP@G-PP NPs exhibit significant advantages in targeting ability, drug delivery and penetration efficiency, and safety. Notably, their excellent stability provides a solid guarantee for the treatment process. The biodegradable polymer PLGA was chosen as the main material, benefiting from its easy surface modification and long-circulating capabilities. PLGA

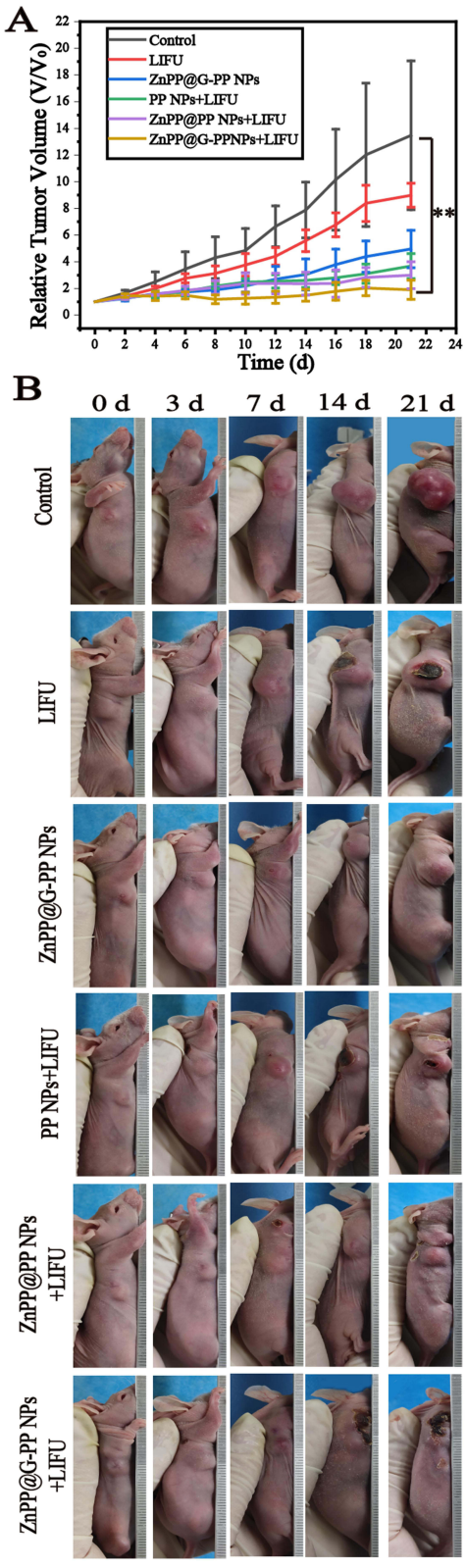

Figure 8 In vivo synergistic tumour therapy. (**A**) Relative tumour growth curve. (**B**) Status maps of 786-O tumour-bearing mice at 0 d, 3 d, 7 d, 14 d,and 21 days after different treatments. (n=3, $^{**}P < 0.01$).

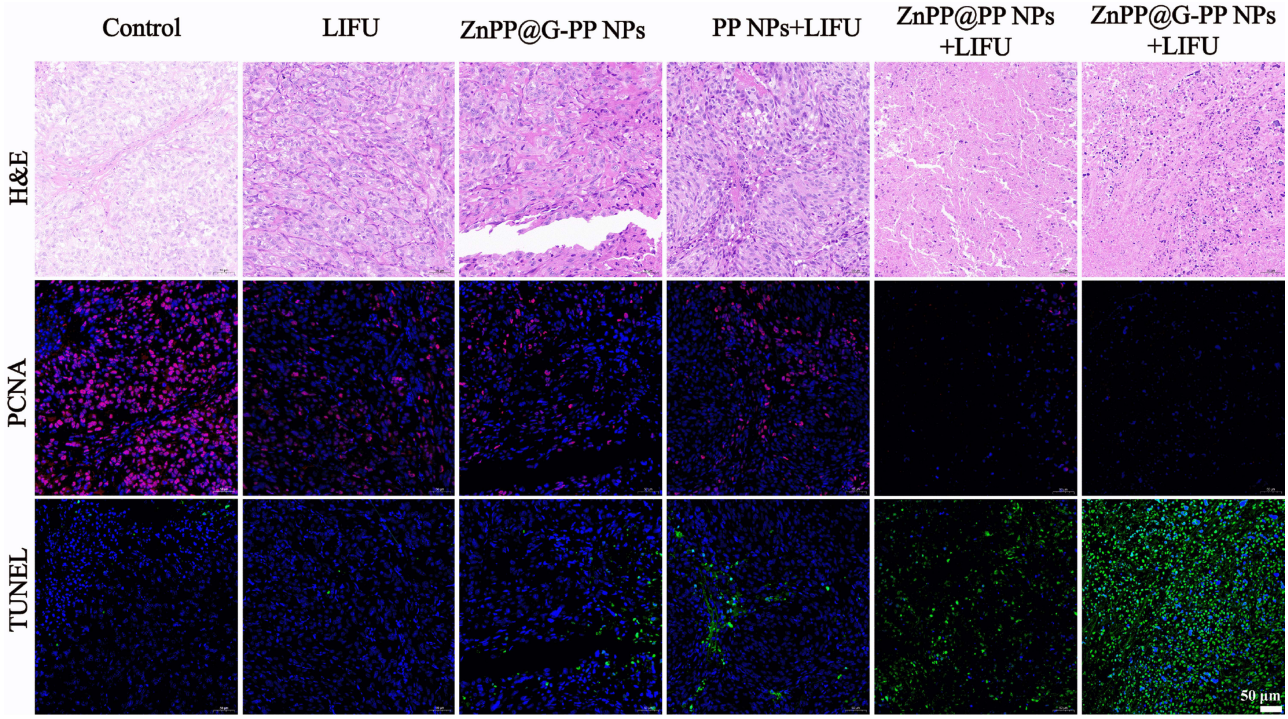

Figure 9 Histological and immunohistochemical examination of H&E, PCNA (red), and TUNEL (green) staining of tumour tissue after different treatments. The scale bar indicates 50 μm.

successfully carries the sonosensitizer ZnPP and is wrapped with PFP as a phase change core, tightly bound to the G250 surface through an amide bond. This design allows NPs to precisely bind to receptors on the surface of tumor cells via their specific ligands, achieving efficient targeted therapy. SDT utilizes the ROS produced by the activation of the sonosensitizer ZnPP to cause damage to tumor cells, achieving a therapeutic effect. Moreover, ZnPP also possesses PA imaging capabilities, further expanding its application in the field of biomedical imaging. Simultaneously, the acoustic phase transformation characteristics exhibited by PFP under LIFU irradiation endow the system with US imaging capabilities. In summary, the rational integration of various material properties in the ZnPP@G-PP NPs nanoplatform not only paves a new way for the precise diagnosis and treatment of RCC but also lays a solid foundation for future clinical applications.

Conclusion

RCC is an aggressive type of malignant tumor, and significant challenges still exist in finding effective treatment options and developing early diagnostic methods. To address this issue, we have designed and developed a sonosensitive targeted nanoplatform (ZnPP@G250-PFP-PLGA NPs) that integrates SDT and UTMD effect. Decorated with the specific G250 antibody, this platform not only achieves efficient targeted therapy for ccRCC but also promotes the efficient accumulation of NPs in the tumor site. Moreover, with the synergistic effect of SDT and UTMD effect, NPs can penetrate more deeply into tumor tissues, significantly enhancing treatment efficiency. This innovation addresses the urgent needs for ccRCC detection and treatment. Compared to the limitations of traditional targeted therapy, our sonosensitive targeted nanoplatform promises to effectively inhibit tumor growth while leaving behind no side effects. In addition, these NPs have photoacoustic and ultrasonic imaging capabilities, enabling multimodal imaging for precise diagnosis and treatment monitoring. Therefore, this strategy provides a solid foundation for future research on ccRCC treatment and opens up new therapeutic directions.

Animal Ethics Statement

In vitro experiments were performed at the Chongqing Key Laboratory of Ultrasonic Molecules.Our animal experiments were performed at the Basic Medical Sciences of Jilin University. Ethical approval was provided by the Basic Medical Sciences of Jilin University, and our laboratory animal welfare protocol followed the JLU-2024-0301 Laboratory Animal - Guideline for ethical review of animal welfare and the Guide for the Care and Use of Laboratory Animals: Eighth Edition.

Acknowledgments

The authors thank Chongqing Key Laboratory of Ultrasonic Molecules for providing the laboratory. This work was supported by the Department of Science and Technology of Jilin Province (grant number 20200201313JC).

Disclosure

The authors report no conflicts of interest in this work.

References

1. Lih TM, Cho KC, Schnaubelt M, Hu Y, Zhang H. Integrated glycoproteomic characterization of clear cell renal cell carcinoma. *Cell Rep*. 2023;42(5):112409. doi:10.1016/j.celrep.2023.112409
2. Wang J, Yin X, He W, Xue W, Zhang J, Huang Y. SUV39H1 deficiency suppresses clear cell renal cell carcinoma growth by inducing ferroptosis. *Acta Pharm Sin B*. 2021;11(2):406–419. doi:10.1016/j.apsb.2020.09.015
3. Capitanio U, Montorsi F. Renal cancer. *Lancet*. 2016;387(10021):894–906. doi:10.1016/S0140-6736(15)00046-X
4. Hsieh JJ, Purdue MP, Signoretti S, et al. Renal cell carcinoma. *Nat Rev Dis Primers*. 2017;3(1):17009. doi:10.1038/nrdp.2017.9
5. Chevrier S, Levine JH, Zanotelli VRT, et al. An Immune Atlas of Clear Cell Renal Cell Carcinoma. *Cell*. 2017;169(4):736–749.e18. doi:10.1016/j.cell.2017.04.016
6. Sykes EA, Dai Q, Sarsons CD, et al. Tailoring nanoparticle designs to target cancer based on tumor pathophysiology. *Proc Natl Acad Sci U S A*. 2016;113(9):E1142–51. doi:10.1073/pnas.1521265113
7. Lammers T, Kiessling F, Ashford M, Hennink W, Crommelin D, Storm G. Cancer nanomedicine: is targeting our target? *Nat Rev Mater*. 2016;1(9):16069. doi:10.1038/natrevmats.2016.69
8. Dong X, Liu HJ, Feng HY, et al. Enhanced Drug Delivery by Nanoscale Integration of a Nitric Oxide Donor To Induce Tumor Collagen Depletion. *Nano Lett*. 2019;19(2):997–1008. doi:10.1021/acs.nanolett.8b04236
9. Yu Z, Wang Y, Xu D, et al. G250 Antigen-Targeting Drug-Loaded Nanobubbles Combined with Ultrasound Targeted Nanobubble Destruction: a Potential Novel Treatment for Renal Cell Carcinoma. *Int J Nanomed*. 2020;15:81–95. doi:10.2147/IJN.S230879
10. Supuran CT. Advances in structure-based drug discovery of carbonic anhydrase inhibitors. *Expert Opin Drug Discov*. 2017;12(1):61–88. doi:10.1080/17460441.2017.1253677
11. Nocentini A, Supuran CT. Carbonic anhydrase inhibitors as antitumor/antimetastatic agents: a patent reviews. *Expert Opin Ther Pat*. 2018;28(10):729–740. doi:10.1080/13543776.2018.1508453
12. Mahon BP, Pinard MA, McKenna R. Targeting carbonic anhydrase IX activity and expression. *Molecules*. 2015;20(2):2323–2348. doi:10.3390/molecules20022323
13. Muselaers CH, Rijpkema M, Bos DL, et al. Radionuclide and Fluorescence Imaging of Clear Cell Renal Cell Carcinoma Using Dual Labeled Anti-Carbonic Anhydrase IX Antibody G250. *J Urol*. 2015;194(2):532–538. doi:10.1016/j.juro.2015.02.041
14. Domingues C, Santos A, Alvarez-Lorenzo C, et al. Where Is Nano Today and Where Is It Headed? A Review of Nanomedicine and the Dilemma of Nanotoxicology. *ACS Nano*. 2022;16(7):9994–10041. doi:10.1021/acsnano.2c00128
15. Stylianou A, Mpekris F, Voutouri C, et al. Nanomechanical properties of solid tumors as treatment monitoring biomarkers. *Acta Biomater*. 2022;154:324–334. doi:10.1016/j.actbio.2022.10.021
16. Kingston BR, Lin ZP, Ouyang B, et al. Specific Endothelial Cells Govern Nanoparticle Entry into Solid Tumors. *ACS Nano*. 2021;15(9):14080–14094. doi:10.1021/acsnano.1c04510
17. Gu L, Duan Z, Li X, et al. Enzyme-triggered deep tumor penetration of a dual-drug nanomedicine enables an enhanced cancer combination therapy. *Bioact Mater*. 2023;26:102–115. doi:10.1016/j.bioactmat.2023.02.015
18. Jain RK. Delivery of molecular and cellular medicine to solid tumors. *Adv Drug Deliv Rev*. 2012;64(Suppl):353–365. doi:10.1016/j.addr.2012.09.011
19. Yhee JY, Jeon S, Yoon HY, et al. Effects of tumor microenvironments on targeted delivery of glycol chitosan nanoparticles. *J Control Release*. 2017;267:223–231. doi:10.1016/j.jconrel.2017.09.015
20. Zhou L, Huo M, Qian X, et al. Autophagy blockade synergistically enhances nanosonosensitizer-enabled sonodynamic cancer nanotherapeutics. *J Nanobiotechnology*. 2021;19(1):112. doi:10.1186/s12951-021-00855-y
21. Son S, Kim JH, Wang X, et al. Multifunctional sonosensitizers in sonodynamic cancer therapy. *Chem Soc Rev*. 2020;49(11):3244–3261. doi:10.1039/C9CS00648F
22. Zhu L, Zhao H, Zhou Z, et al. Peptide-Functionalized Phase-Transformation Nanoparticles for Low Intensity Focused Ultrasound-Assisted Tumor Imaging and Therapy. *Nano Lett*. 2018;18(3):1831–1841. doi:10.1021/acs.nanolett.7b05087
23. Lee S, Han H, Koo H, et al. Extracellular matrix remodeling in vivo for enhancing tumor-targeting efficiency of nanoparticle drug carriers using the pulsed high intensity focused ultrasound. *J Control Release*. 2017;263:68–78. doi:10.1016/j.jconrel.2017.02.035

24. Choi Y, Han H, Jeon S, et al. Deep Tumor Penetration of Doxorubicin-Loaded Glycol Chitosan Nanoparticles Using High-Intensity Focused Ultrasound. *Pharmaceutics*. 2020;12(10):974. doi:10.3390/pharmaceutics12100974
25. Liu JX, Shang TT. Wang FJ. et al. Low-intensity focused ultrasound (LIFU)-induced acoustic droplet vaporization in phase-transition perfluoropentane nanodroplets modified by folate for ultrasound molecular imaging. Int. *J Nanom*. 12:911–923. doi:10.2147/IJN.S122667
26. Gong YP, Wang ZG, Dong G. Dong GF. et al. Low-intensity focused ultrasound mediated localized drug delivery for liver tumors in rabbits. *Drug Deliv*. 2016;23(7):2280–2289. doi:10.3109/10717544.2014.972528
27. Solovieva AO, Vorotnikov YA, Trifonova KE, et al. Cellular internalisation, bioimaging and dark and photodynamic cytotoxicity of silica nanoparticles doped by {Mo6I8}4+ metal clusters. *J Mater Chem B*. 2016;4(28):4839–4846. doi:10.1039/C6TB00723F
28. Zhao H, Wu M, Zhu L, et al. Cell-penetrating Peptide-modified Targeted Drug-loaded Phase-transformation Lipid Nanoparticles Combined with Low-intensity Focused Ultrasound for Precision Theranostics against Hepatocellular Carcinoma. *Theranostics*. 2018;8(7):1892–1910. doi:10.7150/thno.22386
29. Huang Y, Ouyang W, Lai Z, et al. Nanotechnology-enabled sonodynamic therapy against malignant tumors. *Nanoscale Adv*. 2024;6(8):1974–1991. doi:10.1039/D3NA00738C
30. Kopechek JA, Carson AR, McTiernan CF. McTieman CF. et al. Ultrasound Targeted Microbubble Destruction-Mediated Delivery of a Transcription Factor Decoy Inhibits STAT3 Signaling and Tumor Growth. Theranostics. 2015. *Theranostics*. 2015;5(12):1378–1387. doi:10.7150/thno.12822
31. Carson AR, McTieman CF, Lavery L, et al. Ultrasound-targeted microbubble destruction to deliver siRNA cancer therapy. *Cancer Res*. 2012;72(23):6191–6199. doi:10.1158/0008-5472.CAN-11-4079
32. Hu C, Hou B, Hu C, Hou B, Xie S. Application of nanosonosensitizer materials in cancer sono-dynamic therapy. *RSC Adv*. 2022;12(35):22722–22747. doi:10.1039/D2RA03786F
33. Jiang Z, Xiao W, Fu Q. Stimuli responsive nanosonosensitizers for sonodynamic therapy. *J Control Release*. 2023;361:547–567. doi:10.1016/j.jconrel.2023.08.003
34. Chen S, Wang J, Liao H, et al. M1 Macrophage-Derived Sonoresponsive Nanoparticles for Sonodynamic Anticancer Therapy. *Int J Nanomed*. 2022;17:4725–4741. doi:10.2147/IJN.S381170
35. Hsu JC, Barragan D, Tward AE, et al. A Biodegradable "One-For-All" Nanoparticle for Multimodality Imaging and Enhanced Photothermal Treatment of Breast Cancer. *Adv Healthc Mater*. 2023;20:e2303018.
36. Ho YJ, Huang CC, Fan CH, Liu HL, Yeh CK. Ultrasonic technologies in imaging and drug delivery. *Cell Mol Life Sci*. 2021;78(17–18):6119–6141. doi:10.1007/s00018-021-03904-9
37. He Y, Chen QW, Yu JX, et al. Yeast cell membrane-camouflaged PLGA nanoparticle platform for enhanced cancer therapy. *J Control Release*. 2023;359:347–358. doi:10.1016/j.jconrel.2023.05.043
38. Qi F, Wu J, Sun G, Nan F, Ngai T, Ma G. Systematic studies of Pickering emulsions stabilized by uniform-sized PLGA particles: preparation and stabilization mechanism. *J Mater Chem B*. 2014;2(43):7605–7611. doi:10.1039/C4TB01165A
39. Albert C, Beladjine M, Tsapis N, Fattal E, Agnely F, Huang N. Pickering emulsions: preparation processes, key parameters governing their properties and potential for pharmaceutical applicaWang Qtions. *J Control Release*. 2019;309:302–332. doi:10.1016/j.jconrel.2019.07.003
40. Wang Q, Sui G, Wu X, et al. A sequential targeting nanoplatform for anaplastic thyroid carcinoma theranostics. *Acta Biomater*. 2020;102:367–383. doi:10.1016/j.actbio.2019.11.043
41. Tong Y, Wang Y, Bian S, et al. Incorporating Ag@RF core-shell nanomaterials into the thin film nanocomposite membrane to improve permeability and long-term antibacterial properties for nanofiltration. *Sci Total Environ*. 2022;839:156231. doi:10.1016/j.scitotenv.2022.156231
42. Zhao Y, Shi D, Guo L, et al. Ultrasound targeted microbubble destruction-triggered nitric oxide release via nanoscale ultrasound contrast agent for sensitizing chemoimmunotherapy. *J Nanobiotechnology*. 2023;21(1):35. doi:10.1186/s12951-023-01776-8
43. Zheng Y, Zhang Y, Ao M, et al. Hematoporphyrin encapsulated PLGA microbubble for contrast enhanced ultrasound imaging and sonodynamic therapy. *J Microencapsul*. 2012;29(5):437–444. doi:10.3109/02652048.2012.655333
44. Chen KW, Hsu PH, Huang HL, et al. Targeting nanoparticle-conjugated microbubbles combined with ultrasound-mediated microbubble destruction for enhanced tumor therapy. *Pharmacol Res*. 2022;186:106532. doi:10.1016/j.phrs.2022.106532
45. Yu Z, Hu M, Li Z, et al. Anti-G250 nanobody-functionalized nanobubbles targeting renal cell carcinoma cells for ultrasound molecular imaging. *Nanotechnology*. 2020;31(20):205101. doi:10.1088/1361-6528/ab7040
46. Chen J, Li J, Zhong C, et al. Nanobody-loaded nanobubbles targeting the G250 antigen with ultrasound/photoacoustic/fluorescence multimodal imaging capabilities for specifically enhanced imaging of RCC. *Nanoscale*. 2023;16(1):343–359. doi:10.1039/D3NR04097F
47. Zhong C, Chen J, Ling Y, et al. Indocyanine Green-Loaded Nanobubbles Targeting Carbonic Anhydrase IX for Multimodal Imaging of Renal Cell Carcinoma. *Int J Nanomed*. 2023;18:2757–2776. doi:10.2147/IJN.S408977
48. Song X, Feng L, Liang C, Yang K, Liu Z. Ultrasound Triggered Tumor Oxygenation with Oxygen-Shuttle Nanoperfluorocarbon to Overcome Hypoxia-Associated Resistance in Cancer Therapies. *Nano Lett*. 2016;16(10):6145–6153. doi:10.1021/acs.nanolett.6b02365
49. Kim HW, Greenburg AG. Artificial oxygen carriers as red blood cell substitutes: a selected review and current status. *Artif Organs*. 2004;28(9):813–828. doi:10.1111/j.1525-1594.2004.07345.x
50. Yuan F, Leunig M, Huang SK, Berk DA, Papahadjopoulos D, Jain RK. Microvascular permeability and interstitial penetration of sterically stabilized (stealth) liposomes in a human tumor xenograft. *Cancer Res*. 1994;54(13):3352–3356.
51. Li M, Zhang Y, Zhang Q, Li J. Tumor extracellular matrix modulating strategies for enhanced antitumor therapy of nanomedicines. *Mater Today Bio*. 2022;16:100364. doi:10.1016/j.mtbio.2022.100364
52. Cao X, Li M, Liu Q, Zhao J, Lu X, Wang J. Inorganic Sonosensitizers for Sonodynamic Therapy in Cancer Treatment. *Small*. 2023;19(42):e2303195. doi:10.1002/smll.202303195
53. Duan W, Li B, Zhang W, et al. Two-photon responsive porphyrinic metal-organic framework involving Fenton-like reaction for enhanced photodynamic and sonodynamic therapy. *J Nanobiotechnology*. 2022;20(1):217. doi:10.1186/s12951-022-01436-3
54. Hou J, Zhou J, Chang M, et al. LIFU-responsive nanomedicine enables acoustic droplet vaporization-induced apoptosis of macrophages for stabilizing vulnerable atherosclerotic plaques. *Bioact Mater*. 2022;16:120–133. doi:10.1016/j.bioactmat.2022.02.022
55. Liu J, Shang T, Wang F, et al. Low-intensity focused ultrasound (LIFU)-induced acoustic droplet vaporization in phase-transition perfluoropentane nanodroplets modified by folate for ultrasound molecular imaging. *Int J Nanomed*. 2017;12:911–923. doi:10.2147/IJN.S122667

56. Liang Y, Zhang M, Zhang Y, Zhang M. Ultrasound Sonosensitizers for Tumor Sonodynamic Therapy and Imaging: a New Direction with Clinical Translation. *Molecules*. 2023;28(18):6484. doi:10.3390/molecules28186484
57. Wang G, Song L, Hou X, et al. Surface-modified GVs as nanosized contrast agents for molecular ultrasound imaging of tumor. *Biomaterials*. 2020;236:119803. doi:10.1016/j.biomaterials.2020.119803
58. Oosterwijk-Wakka JC, Boerman OC, Mulders PF, Oosterwijk E. Application of monoclonal antibody G250 recognizing carbonic anhydrase IX in renal cell carcinoma. *Int J Mol Sci*. 2013;14(6):11402–11423. doi:10.3390/ijms140611402
59. Zatovicova M, Jelenska L, Hulikova A, et al. Monoclonal antibody G250 targeting CA IX: binding specificity, internalization and therapeutic effects in a non-renal cancer model. *Int J Oncol*. 2014;45(6):2455–2467. doi:10.3892/ijo.2014.2658
60. Luo M, Cheng W, Zeng X, Mei L, Liu G, Deng W. Folic Acid-Functionalized Black Phosphorus Quantum Dots for Targeted Chemo-Photothermal Combination Cancer Therapy. *Pharmaceutics*. 2019;11(5):242. doi:10.3390/pharmaceutics11050242